Linearity Analysis of CMOS Parametric Upconverters

ZHIXING ZHAO[1], **SEBASTIAN MAGIEROWSKI**[2], **(Member, IEEE),**
AND LEONID BELOSTOTSKI[1], **(Senior Member, IEEE)**
[1]Department of Electrical and Computer Engineering, University of Calgary, Calgary, AB T2N 1N4, Canada
[2]Department of Electrical Engineering and Computer Science, Lassonde School of Engineering, York University, Toronto, ON M3J 1P3, Canada

Corresponding author: Zhixing Zhao (zhaoz@ucalgry.ca)

ABSTRACT This paper applies a conversion matrix approach to the linearity analysis of a varactor-based 36-GHz CMOS parametric upconverter. The nonlinear model of the upconverter is explained and derived. The comparison between the measurements, simulations, and theoretical calculation is presented to show excellent agreements: 0.5- and 1.5-dB differences in conversion gains for lower-sideband and upper-sideband upconversion, and less than 2.9-dB in both IIP_2 and IIP_3 when converting a 1-GHz signal to 36-GHz output.

INDEX TERMS CMOS, conversion matrix, internmodulation distortion, IIP2, IIP3, parametric mixer, upconverter linearity.

I. INTRODUCTION

The term ''parametric circuit'' typically denotes a system that utilizes a nonlinear-reactance device to realize signal amplification and frequency mixing. This technique can trace its use in communications to at least the turn of the 20th century [1] and, among many reports, was famously the subject of radar research at the MIT radiation laboratory [2], [3].

Capable of achieving high frequency power gain, superior to their transistor contemporaries, parametric circuits, and research into their design, prospered at mid-century [4]–[10]. However, the traditional parametric circuit, typically being centred around two-terminal varactor devices, is bilateral in nature, a characteristics that significantly complicates its design. Following the emergence of high-mobility transistors and the progressive improvement of their silicon counterparts, parametric circuit research focused towards specialized uses with extreme performance requirements in the sub-millimeter-wave range [11]–[32] and on optical applications [33]–[37].

However, the on-going motivation to provide broadband services via expanding wireless spectrum availability and to enable more sophisticated sensing modalities in the millimeter and sub-millimeter domain have helped to re-opened opportunities for parametric circuits [30], [38]–[43]. In particular, CMOS-based parametric circuits have started to draw attention in both millimeter and sub-millimeter region

The associate editor coordinating the review of this manuscript and approving it for publication was Dušan Grujić.

applications [32], [40], [41], [44]–[54]. With these advances, the need to update design insights for modern parametric circuits in modern electronic technologies has arisen, a challenge addressed in this paper.

Given that the incumbent focus in parametric research has been towards space-borne applications in the sub-millimeter-wave regime [12]–[16], [18], [20] with emphasis related to frequency multiplication and downconversion of low-power signals, design for linear parametric signal transmission has not been strongly emphasized.

At lower frequencies, researchers have modelled the transducer gain, gain compression point, power efficiency, stability, as well as linearity of discrete parametric circuits, including degenerate parametric amplifiers and upconverters [55]–[68], however linearity analyses of CMOS-based continuous-time parametric upconverters in the millimeter-wave range remain scarce.

In a networked communication system, in-band and adjacent-band interferers can significantly degrade performance due to transceiver nonlinearities. These degradations include dc shifts, unwanted in-band signal generation, etc. The figures of merit for characterizing linearity or the immunity of systems to interference are the intermodulation products (IMs), which are defined as the ratios of the signal levels of the main tones to the levels of the unwanted frequency components generated by circuit nonlinearities. The IMs are also used to define other figures of merit, such as the second-order intercept point (IP_2) and the third-order intercept point (IP_3), which are, respectively, associated

with the second-order and third-order nonlinearities of the system.

The most relevant parametric topology to consider in light of these metrics is the upconverter. Since a linearity analysis of such parametric circuits has not been previously developed, the goal of this work is to we investigate this circuit linearity in the context of a CMOS technology. To the authors' knowledge, this is among the first works to detail a linearity analysis for a continuous-time CMOS parametric upconverter aimed for operation in the millimeter-wave range.

In particular, we present a curve interpolation for the linearity analysis and its substantiation with measured results from a 36-GHz CMOS parametric upconverter. Our report starts by outlining our assumptions for the circuit analysis in Section II followed by the development of a suitable nonlinear model of the CMOS varactor in Section III. Next, Section IV applies small-signal analyses to the 1st-, 2nd-, and 3rd-order equivalent circuits of a parametric upconverter to calculate input-referred IP_2 (i.e. IIP_2), and input-referred IP_3 (i.e. IIP_3); the validity of our approach is discussed in the context of measurement results presented in Section VI.

II. PARAMETRIC UPCONVERTER ANALYSIS SET-UP

The nonlinear capacitive reactance, the varactor, forming the heart of a parametric upconverter is positioned in the circuit as shown in Fig. 1. As indicated, the upconverter harmonic input signal, V_{IF}, at angular *intermediate frequency* ω_{IF} is mixed with ω_P to an angular *radio frequency* ω_{RF} signal appearing across the output impedance Z_{rf}. This frequency upconversion is accomplished by exciting the varactor with the PUMP harmonic current source I_P at angular *pump frequency* ω_P.
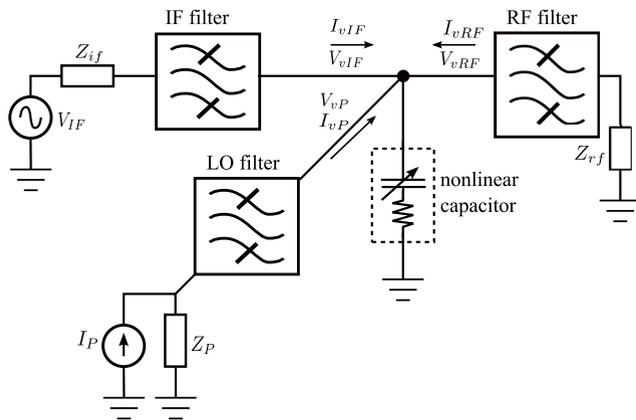

FIGURE 1. Fundamental circuit description of the parametric upconverter and the reactive component presence therein. The IF, RF, and LO filters are assumed ideal and pass only the IF, RF, and LO frequencies respectively.

The nonlinear capacitor comprising the functional core of the circuit is modelled as a linear resistor connected in series with a voltage-controlled capacitor, an approximation previously analyzed in [69]. The value of the capacitance is controlled by the voltage across the nonlinear element.

In the figure, the V_{vIF} and I_{vIF} are, respectively, the voltage and current across and through the entire varactor model

(i.e. the series-connected resistor and voltage-controlled capacitor) at ω_{IF}. Similar definitions apply to V_{vRF}, I_{vRF}, V_{vP} and I_{vP}. The IF and RF filters are assumed lossless and only pass signals at frequencies corresponding to their respective pass bands.

In the following analyses, the signals are assumed to satisfy the following conditions:

1) the two-tone input frequencies $\omega_{IF1} \approx \omega_{IF2} \approx \omega_{IF}$;
2) $\omega_{IF1} > \omega_{IF2}$;
3) the amplitudes of the input tones at ω_{IF1} and ω_{IF2} are identical, i.e. $V_{IF1} = V_{IF2} = V_{IF}$;
4) the amplitude of the PUMP signal at ω_P is much larger than the input tones at ω_{IF1} and ω_{IF2} so that the system is assumed to work in a weakly nonlinear region;
5) the output frequencies are $\omega_{RF1/RF2} = \omega_P + \omega_{IF1/IF2}$ for an upper-sideband (USB) parametric upconverter configuration and the output frequencies are $\omega_{RF1/RF2} = \omega_P - \omega_{IF1/IF2}$ for a lower-sideband (LSB) parametric upconverter configuration;
6) the signal frequency components $\omega_P + 2\omega_{IF1} - \omega_{IF2} \approx \omega_{RF}$ and therefore pass through the RF filter;
7) the PUMP signal and the two input signals are uncorrelated;
8) all input signals are periodic.

According to [70], [71], in order to characterize the linearity of an upconverter, two equal-amplitude spectrally-proximate signals ω_{IF1} and ω_{IF2} are applied to the circuit's IF input port. When mixed with the PUMP signal, these two inputs are translated to ω_{RF1} and ω_{RF2}. As shown in Fig. 2, these are joined by other frequency combinations due to the upconverter nonlinearity.
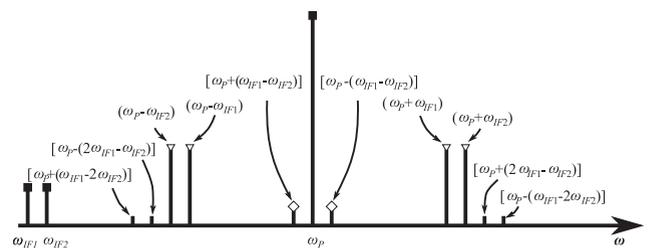

FIGURE 2. Spectral distribution of the nonlinear upconverter signals for the analysis under consideration. It is assumed that all frequencies of interest can be equally delivered to the output. Subscripts outside the square brackets indicate the mixing product order.

In Fig. 2, the frequency components corresponding to the same order (i.e. 1st, 2nd, and 3rd-order signals) are drawn at the same amplitude, a consequence of the assumption of ideal filters. This assumption is implicitly present in the remainder of our analysis. The plurality of output tones implies that, to quantify IIP_2 and IIP_3, more than one frequency could be used. In general this is true, and the choice of output frequency (or even frequencies) for the calculation of IIP_2 and IIP_3 should reflect the specifics of the application and the architecture of the circuit under test.

In the following we only consider the standard case which accounts for just one of the frequency components at the 2nd- and 3rd-order mixing products, respectively, shown in Fig. 2. However, extending the calculation to account for a plurality of tones simply requires a re-application of the methods to follow at those frequencies of interest.

Based on the preceding discussion and [70], the IIP_2 and IIP_3 linearity metrics are calculated as

$$IIP_2 = \frac{P_{out}(\omega_P + \omega_{IF1})}{P_{out}[\omega_P + (\omega_{IF1} - \omega_{IF2})]} P_{in}(\omega_{IF}) \tag{1a}$$

and

$$IIP_3 = \left\{ \frac{P_{out}(\omega_P + \omega_{IF1})}{P_{out}[\omega_P + (2\omega_{IF1} - \omega_{IF2})]} \right\}^{\frac{1}{2}} P_{in}(\omega_{IF}) \tag{1b}$$

where $P_{in}(\omega_{IF})$ is the input operating power at ω_{IF1} or ω_{IF2} and may be expressed as

$$P_{in}(\omega_{IF}) = \frac{1}{2}|I_{vIF}|^2 \Re(Z_{if}) \tag{2}$$

and where $P_{out}(\omega)$ is the power delivered to the output load at frequency ω and may be expressed as

$$P_{out}(\omega) = \frac{1}{2} \frac{|V_{vRF}(\omega)|^2}{\Re[Z_{rf}(\omega)]} = \frac{1}{2}|I_{vRF}|^2 \Re[Z_{rf}(\omega)]. \tag{3}$$

To capture the IIP_2 and IIP_3 expressions in terms of relevant circuit design parameters, the output powers at the frequencies of interest noted in (1a) and (1b) must be detailed using circuit analysis. This effort requires the calculation of Z_{rf}'s RF voltage and current which, in turn, depend on the manner in which the IF and PUMP signals are mixed across the varactor. We now discuss this mechanism in terms of the circuit and varactor model characteristics of Figs. 1 and 3, respectively.
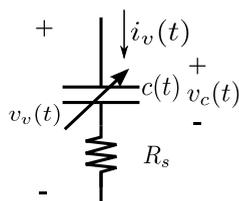

FIGURE 3. Varactor model and its terminal characteristics.

III. VARACTOR NONLINEAR MODEL

The varactor model is illustrated in Fig. 3, which shows it consists of voltage-controlled capacitor in series connected with a linear resistor. The net voltage $v_v(t)$ across a parametric upconverter's varactor can be expressed as

$$v_v(t) = v_c(t) + R_s i_v(t) \tag{4}$$

where $i_v(t)$ is the current through the varactor and $v_c(t)$ is the voltage drop across the voltage-controlled capacitor.

The varactor device properties are linked to these terms via

$$v_c(t) = q_c(t)/c(t) = q_c(t)s(t) \tag{5}$$

where $q_c(t)$ is the charge on the capacitor and $s(t) \equiv c(t)^{-1}$ is the elastance. The time-domain terms $v_v(t)$, $v_c(t)$, and $i_v(t)$ in (4) and (5) contain all possible frequency combinations including the frequencies of large signals, small signals, and their frequency mixtures. According to assumption 7), by isolating the large signals and small signals from the expressions, the following set of equations are obtained

$$q_c(t) = q_P(t) + q(t), \tag{6}$$
$$v_v(t) = v_P(t) + v(t), \tag{7}$$
$$i_v(t) = i_P(t) + i(t) \tag{8}$$

where the subscript P denotes the large, PUMP-induced signal, while $v(t)$, $i(t)$, and $q(t)$ indicate the small-signal contributors that contain the IF and RF signal components as well as their intermodulation products.

Invoking assumption 4), (5) may be stated as a Taylor or Volterra series expansion around the PUMP signal. The Volterra kernels and the Taylor-series coefficients are related through combinations of circuit reactive-component impedances [72]. As there is only one nonlinear component in the parametric mixer, the Taylor series expansion is selected in this work to avoid potential convergence problems associated with Volterra analysis of circuits driven by large signals, such as the PUMP. Consequently, via (6)–(8), the small-signal component of $v_v(t)$ across the varactor can be formulated with

$$v(t) = s_1(t)q(t) + s_2(t)q^2(t) + s_3(t)q^3(t) + \ldots + R_s i(t) \tag{9}$$

where $s_1(t)$, $s_2(t)$, and $s_3(t)$ are the Taylor series coefficients

$$s_1(t) = \left.\frac{d[v_c(t)]}{dq_c}\right|_{q_P} \tag{10}$$

$$s_2(t) = \left.\frac{1}{2}\frac{d^2[v_c(t)]}{dq_c^2}\right|_{q_P} \tag{11}$$

$$s_3(t) = \left.\frac{1}{6}\frac{d^3[v_c(t)]}{dq_c^3}\right|_{q_P} \tag{12}$$

all of which are solely determined by the PUMP signal.

Since we are only interested in IIP_2 and IIP_3, the order of the Taylor expansion is restricted to three and the resulting small-signal voltage on the varactor in (9) can be rewritten as

$$v(t) \approx s_1(t) \int i(t)dt + s_2(t) \left(\int i(t)dt \right)^2 + s_3(t) \left(\int i(t)dt \right)^3 + R_s i(t). \tag{13}$$

where $i(t)$ is the small-signal current through the varactor as presented in (8).

Continuing our interest in only the second and third-order intercepts, this current is also approximated by components up to third order, that is:

$$i(t) \approx i_1(t) + i_2(t) + i_3(t) \tag{14}$$

where the subscript effectively indicates small-signal current at the order of the mixing product in time domain.

Rearranging (13) according to the relationship noted by (14), the 1st-, 2nd-, and 3rd-order small-signal voltage components across the varactor assume the relations:

$$v_1(t) = s_1(t) \int i_1(t)dt + R_s i_1(t) \tag{15a}$$

$$v_2(t) = s_1(t) \int i_2(t)dt + R_s i_2(t) + v_{2s}(t) \tag{15b}$$

$$v_3(t) = s_1(t) \int i_3(t)dt + R_s(t)i_3(t) + v_{3s}(t) \tag{15c}$$

where the varactor's 2nd- and 3rd-order nonlinear component contributions are encapsulated by $v_{2s}(t)$ and $v_{3s}(t)$, each of these being expressible with

$$v_{2s}(t) = s_2(t)\left(\int i_1(t)dt\right)^2 \tag{16a}$$

$$v_{3s}(t) = 2s_2(t)\int i_1(t)dt \int i_2(t)dt$$
$$+ s_3(t)\left(\int i_1(t)dt\right)^3. \tag{16b}$$

Of note is that $v_{2s}(t)$ and $v_{3s}(t)$ contain all the possible frequency combinations that result in 2nd- and 3rd-order mixing products at the upconverter output. They are induced voltage sources due to the nonlinearity of the device. Among the tones generated by these unwanted nonlinear voltage sources are those present at $[\omega_P + (\omega_{IF1} - \omega_{IF2})]$ (from v_{2s}) and $[\omega_P + (2\omega_{IF1} - \omega_{IF2})]$ (from v_{3s}). These in particular bear influence on the upconverter linearity as noted in (1a) and (1b), respectively. Therefore, (15b) indicates elevated 2nd-order output power due to v_{2s}, leading to a lower *IIP2* as implied by (1a). Similarly, (16b) and (1b) imply that the increased 3rd-order output power due to v_{3s} degrades *IIP3* performance.

Not surprisingly, (16) demonstrates that higher-order voltages across our varactor are, in part, related to the lower-order currents flowing through it. For example, the 3rd-order nonlinear voltage v_{3s} in (16b) is partly induced by the combination of two different mixing mechanisms. The first term, $2s_2 \int i_1 dt \int i_2\, dt$, known as the "second-order interaction", is the result of mixing between 2nd-order intermodulation products (e.g. signals at $\omega_P + \omega_{IF1} - \omega_{IF2}$ and $\omega_P + 2\omega_{IF1}$) of the two inputs at ω_{IF1} and ω_{IF2}. The second term, $s_3(\int i_1 dt)^3$, on the other hand, suggests that the 3rd-order nonlinearity degradation also derives from the direct mixture of the 1st-order input signals without the generation of an intermediate 2nd-order signal. Similar observations are also drawn in transistor-based LNA circuits [73], [74] as well as certain MOS varactor-based tripler topologies [75].

With the derivation of (15) and (16) we see that a nonlinear circuit model of the varactor can be split into three parts as organized in Fig. 4. Each part can be used to independently derive nonlinear signal terms and we exploit this partition in the following section to derive expressions for intercept point metrics.
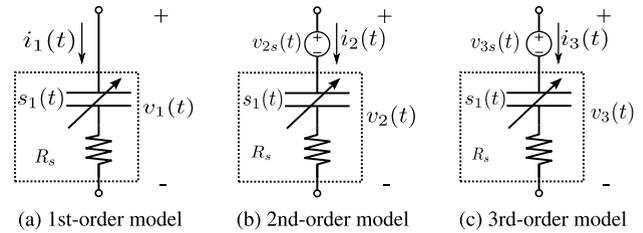

FIGURE 4. Three equivalent circuit models for separately examining varactor nonlinearity components. The subscripts of the currents and voltages indicate the order of the nonlinearity.
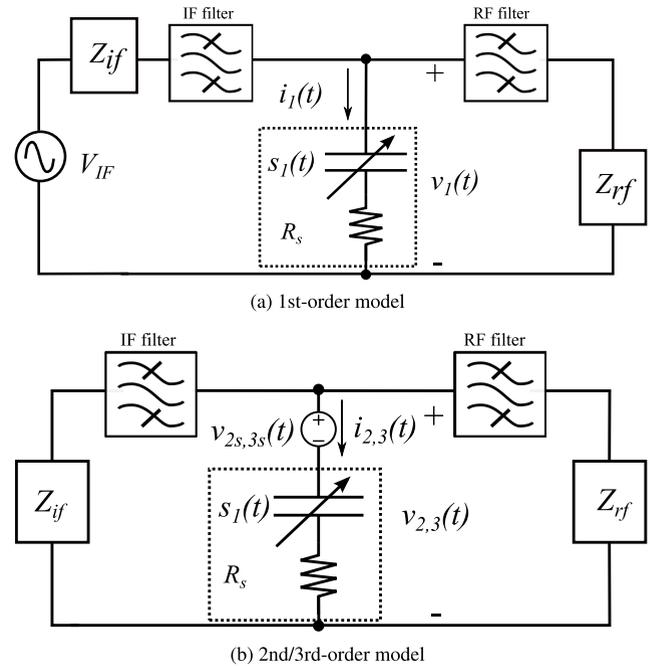

FIGURE 5. Pumped equivalent nonlinear parametric upconverter circuit models. The subscripts of the currents and voltages indicate the order of the nonlinearity.

IV. DERIVATION OF *IIP2* AND *IIP3*

As mentioned previously, the derivation of *IIP2* and *IIP3* boils down to the calculation of the voltage or current through the upconverter's load impedance at the frequency of interest. To do so, we need to derive the upconverter's Thevenin equivalent circuits at each frequency of interest. We do this presently with the assistance of the nonlinear varactor model developed in the previous section.

According to the models in Fig. 4, the upconverter circuit of Fig. 1 can be reduced to the equivalent schematics shown in Fig. 5. In this figure, the PUMP signal is effectively captured by the Taylor series coefficients given in (10) to (12). Thus, this nonlinear varactor model is also referred to as a *pumped varactor model* [61], [76] and it allows us to study the parametric upconverter in terms of a two-port circuit. In the following parts of this section, we will discuss the different-order equivalent circuits shown in Fig. 5 and derive their output power expressions separately.

A. FIRST-ORDER SMALL-SIGNAL EQUIVALENCE

To express $P_{out}(\omega_P + \omega_{IF})$, the numerator of (1a) and (1b), in terms of circuit variables we need to derive the Thevenin equivalent output circuit of the 1st-order schematic pictured in Fig. 5a. To obtain this particular harmonic from our time-domain model expression (15a), we employ the Fourier series formulation to yield

$$v_1(t) = \sum_{k=-1}^{1} S_{1,k} e^{jk\omega_P t} \sum_{m=-1}^{1} \frac{I_{m,l}}{j(m\omega_P + \omega_{IF})} e^{j(m\omega_P + \omega_{IF})t}$$

$$+ \sum_{m=-1}^{1} I_{m,l} \cdot R_s \cdot e^{j(m\omega_P + \omega_{IF})t} \qquad (17)$$

where $S_{1,k}$ is the Fourier-coefficient of s_1 at $k\omega_P$ corresponding to the 1st-order Taylor series elastance term and $I_{m,l}$ is the m-th Fourier-coefficient of the varactor $i(t)$ current at $(m\omega_P + \omega_{IF})$ resulting from the input at ω_{IF}. The subscript l conveys that the output corresponds to an input at ω_{IFl} where l is 1 or 2 depending on the input signal of interest. Recall our assumption 1) that $\omega_{IF} \approx \omega_{IFl}$.

Assuming a single harmonic pump, only the Fourier coefficients at $|k| \leq 1$ are retained for the elastance in (17). By definition, the 1st-order circuit only passes dc and signals at $(\omega_P \pm \omega_{IFl})$, hence $|m| \leq 1$.

Separating small-signal voltages and currents at different frequencies results in a frequency-domain impedance matrix — a *conversion matrix* — shown in (18).

$$\begin{bmatrix} V_v(\omega_P + \omega_{IF}) \\ V_v(\omega_{IF}) \\ V_v^*(\omega_P - \omega_{IF}) \end{bmatrix}$$

$$= \begin{bmatrix} R_s + \dfrac{S_{1,0}}{j(\omega_P + \omega_{IF})} & \dfrac{S_{1,1}}{j\omega_{IF}} & 0 \\[2ex] \dfrac{S_{1,1}^*}{j(\omega_P + \omega_{IF})} & R_s + \dfrac{S_{1,0}}{j\omega_{IF}} & \dfrac{-S_{1,1}}{j(\omega_P - \omega_{IF})} \\[2ex] 0 & \dfrac{S_{1,1}^*}{j\omega_{IF}} & R_s - \dfrac{S_{1,0}}{j(\omega_P - \omega_{IF})} \end{bmatrix}$$

$$\times \begin{bmatrix} I_v(\omega_P + \omega_{IF}) \\ I_v(\omega_{IF}) \\ I_v^*(\omega_P - \omega_{IF}) \end{bmatrix} \qquad (18)$$

In the matrix, $S_{1,0}$ is the average elastance of the varactor in the circuit of Fig. 5a and $S_{1,1}$ represents the fundamental harmonic of the 1st-order elastance. Terms in (18) labelled with an asterisk denote complex conjugates.

With (18), the 1st-order upconverter's Thevenin equivalents at the input and output can be derived by applying KCL and KVL in Fig. 5a. As a result, the Fig. 5a representation takes on the form shown in Fig. 6. As in [77], [78], the upconverter's equivalent IF input impedance can be expressed as

$$Z_{gIF,LSB} = Z_v(\omega_{IF})$$

$$- \frac{|S_{1,1}|^2}{\omega_{RF}\omega_{IF}[Z_v^*(\omega_{RF}) + Z_{rf}^*(\omega_{RF})]} \qquad (19a)$$
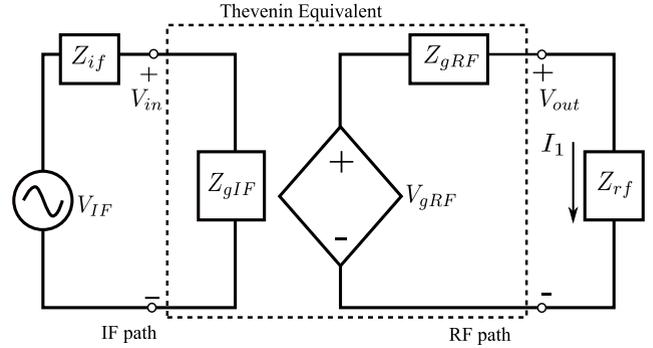

FIGURE 6. First-order Thevenin equivalent circuit for the input and output paths of the parametric upconverter circuit model.

$$Z_{gIF,USB} = Z_v(\omega_{IF})$$

$$+ \frac{|S_{1,1}|^2}{\omega_{RF}\omega_{IF}[Z_v(\omega_{RF}) + Z_{rf}(\omega_{RF})]} \qquad (19b)$$

where $Z_v(\omega) = R_s + S_0/(j\omega)$.

Above, we distinguish the impedance based on the sidebands allowed to excite the RF output. That is, the *LSB* subscript in (19a) denotes variables attendant to the case of a "lower-sideband" upconverter intended to produce an RF output at $(\omega_P - \omega_{IF})$; similarly, the *USB* subscript in (19b) denotes an "upper-sideband" upconverter that produces outputs at $(\omega_P + \omega_{IF})$.

Along identical lines, the equivalent RF output source assumes the forms

$$V_{gRF,LSB} = \frac{-S_{1,1}}{j\omega_{IF}} \frac{v_{IF}^*}{Z_v^*(\omega_{IF}) + Z_{if}^*(\omega_{IF})} \qquad (20a)$$

$$V_{gRF,USB} = \frac{S_{1,1}}{j\omega_{IF}} \frac{v_{IF}}{Z_v(\omega_{IF}) + Z_{if}(\omega_{IF})} \qquad (20b)$$

and the equivalent RF output impedance is

$$Z_{gRF,LSB} = Z_v(\omega_{RF})$$

$$- \frac{|S_{1,1}|^2}{\omega_{RF}\omega_{IF}[Z_v^*(\omega_{IF}) + Z_{if}^*(\omega_{IF})]} \qquad (21a)$$

$$Z_{gRF,USB} = Z_v(\omega_{RF})$$

$$+ \frac{|S_{1,1}|^2}{\omega_{RF}\omega_{IF}[Z_v(\omega_{IF}) + Z_{if}(\omega_{IF})]} \qquad (21b)$$

The expressions (19) to (21) reflect the bilateral properties of the parametric circuit by virtue of Z_{rf}'s influence on the equivalent IF impedance and the simultaneous influence of Z_{if} on the RF equivalent impedance. Also, notable is the possibility of the LSB configuration's equivalent impedances to assume negative real components, another distinctive feature of parametric circuits [4], [77]–[79].

Employing (19)–(21) in an analysis of the circuit in Fig. 6, the output power can be obtained by calculating the current through the load impedance Z_{rf}. Following the definition of IIP_2 and IIP_3 in (1a) and (1b), we continue by focusing on the USB arrangement whose output power can be

calculated as

$$P_{out}(\omega_P + \omega_{IF}) = \frac{1}{2}|I_1(\omega_P + \omega_{IF})|^2 \Re(Z_{rf}) \quad (22)$$

where

$$I_1(\omega_P + \omega_{IF}) = \frac{V_{gRF}(\omega_P + \omega_{IF})}{Z_{gRF}(\omega_P + \omega_{IF1}) + Z_{rf}(\omega_P + \omega_{IF})} \quad (23)$$

in which $V_{gRF}(\omega_P + \omega_{IF}) = V_{gRF,USB}$ and $Z_{gRF}(\omega_P + \omega_{IF}) = Z_{gRF,USB}$.

B. SECOND-ORDER SMALL-SIGNAL EQUIVALENCE AND IIP_2

Continuing the approach outlined at the beginning of Section IV, we now turn to the 2nd-order circuit of Fig. 5b and ultimately to the calculation of its 2nd-order output power at $[\omega_P + (\omega_{IF1} - \omega_{IF2})]$ to achieve the corresponding IIP_2.

Before detailing the IIP_2 calculation we pause to consider the frequencies of interest among the 2nd-order mixing products. According to (1a), it is the nonlinear output power at $[\omega_P + (\omega_{IF1} - \omega_{IF2})]$ that is needed for the derivation of IIP_2. However, among the 2nd-order mixing products, there is another frequency of interest: $(\omega_P + 2\omega_{IF1})$. This latter contributor is needed for the completion of the 3rd-order calculation (Section IV-C) to come. As the reader may recall, (16b) captures the influence of such a 2nd-order component on v_{3s}. Hence, in this section, these two frequencies will both be accounted for respectively, in the following CASE A and B.

CASE A $[\omega_P + (\omega_{IF1} - \omega_{IF2})]$: We start by deriving an expression for V_{2sA}, the phasor of the 2nd-order nonlinear voltage source pictured in Fig. 5b (i.e. the voltage source spectral equivalent of the 2nd-order mixing product at the frequency of interest in CASE A).

Following the methods of Section IV-A, we replace $s_2(t)$ and $i_1(t)$ with their Fourier series equivalents up to first-order harmonics and then substitute these into (16a) to obtain

$$v_{2sA}(t)$$
$$= \sum_{k=-1}^{1} S_{2,k} e^{jk\omega_P t}$$
$$\cdot \frac{1}{4} \left[\sum_{m=-1}^{1} \frac{I_{m,1}}{j(m\omega_P + \omega_{IF1})} e^{j(m\omega_P + \omega_{IF1})t} \right.$$
$$\left. \cdot \sum_{n=-1}^{1} \frac{I_{n,-2}}{j(n\omega_P - \omega_{IF2})} e^{j(n\omega_P - \omega_{IF2})t} \right]$$
$$= \sum_{k=-1}^{1} \sum_{m=-1}^{1} \sum_{n=-1}^{1} \left\{ V_{2sA,k,m,n} \, e^{j[(m+n+k)\omega_P + (\omega_{IF1} - \omega_{IF2})]t} \right\}$$

$$(24)$$

where $v_{2sA}(t)$ indicates the 2nd-order nonlinear voltage source at frequency $[\omega_P + (\omega_{IF1} - \omega_{IF2})]$ and, as before, $I_{m,\pm l}$ denotes the m-th Fourier coefficient corresponding to input tone $\pm\omega_{IFl}$. Aligning corresponding harmonics in (24) leads

to the general relationship

$$V_{2sA,k,m,n} = \frac{1}{4} \frac{S_{2,k} I_{m,1} I_{n,-2}}{-(m\omega_P + \omega_{IF1})(n\omega_P - \omega_{IF2})} \quad (25)$$

As before, we now turn to the derivation of the conversion matrix, which is identical to that derived in Section IV-A save a change in frequency from $(\omega_P - \omega_{IF})$ to $[\omega_P - (\omega_{IF1} - \omega_{IF2})]$ in the case of an LSB upconverter configuration or a change from $(\omega_P + \omega_{IF})$ to $[\omega_P + (\omega_{IF1} - \omega_{IF2})]$ in the case of a USB configuration.

As in Section IV-A, the new 2nd-order conversion matrix description is used to derive the Thevenin equivalent shown in Fig. 7 for the 2nd-order circuit of Fig. 5b. Obviously, the Thevenin equivalent for the 3rd-order parametric upconverter circuit is structurally identical with only changes to the component properties.
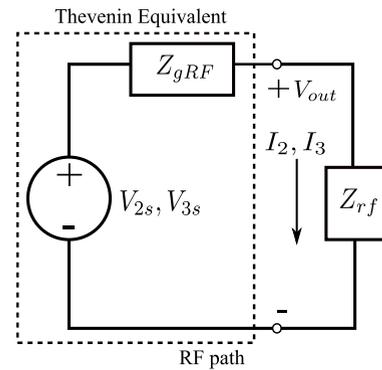

FIGURE 7. Thevenin equivalent circuit for the equivalent 2nd- and 3rd-order parametric upconverter in Fig. 5b. Since the RF path is the only concern in the calculation the IF path equivalent circuit is omitted.

Similar to (21b), the USB configuration's Thevenin equivalent impedance at the RF path assumes the expression

$$Z_{gRF}[\omega_P + (\omega_{IF1} - \omega_{IF2})]$$
$$= Z_v[\omega_P + (\omega_{IF1} - \omega_{IF2})]$$
$$+ \frac{|S_{1,1}|^2}{[\omega_P + (\omega_{IF1} - \omega_{IF2})]\omega_{IF}[Z_v(\omega_{IF}) + Z_{if}(\omega_{IF})]} \quad (26)$$

Then, the current flowing in the RF path at $[\omega_P + (\omega_{IF1} - \omega_{IF2})]$ is calculated to be

$$I_{2sA}[\omega_P + (\omega_{IF1} - \omega_{IF2})]$$
$$= \frac{V_{2sA}}{Z_{gRF}[\omega_P + (\omega_{IF1} - \omega_{IF2})] + Z_{rf}[\omega_P + (\omega_{IF1} - \omega_{IF2})]}. \quad (27)$$

Consequently, the output power for the calculation of IIP_2 coming from the 2nd-order mixing product is

$$P_{out}[\omega_P + (\omega_{IF1} - \omega_{IF2})]$$
$$= \frac{1}{2} |I_{2sA}[\omega_P + (\omega_{IF1} - \omega_{IF2})]|^2 \Re(Z_{rf}). \quad (28)$$

CASE B $(\omega_P + 2\omega_{IF1})$: Using the same method just applied to the derivation of (24), the 2nd-order nonlinear voltage

source at frequency of $(\omega_P + 2\omega_{IF1})$ can be expressed as

$$v_{2sB}(t) = \sum_{k=-1}^{1} \sum_{m=-1}^{1} \sum_{n=-1}^{1} \left\{ V_{2sB,k,m,n} \cdot e^{j[(m+n+k)\omega_P + 2\omega_{IF1}]t} \right\}$$
(29)

where

$$V_{2sB,k,m,n} = \frac{1}{4} \frac{S_{2,k}I_{m,1}I_{n,1}}{-(m\omega_P + \omega_{IF1})(n\omega_P + \omega_{IF1})}$$
(30)

Similar to CASE A, to formulate the conversion matrix, in (18) the RF frequencies are swapped with $(\omega_P - 2\omega_{IF1})$ for an LSB configuration and $(\omega_P + 2\omega_{IF1})$ for a USB configuration, respectively. Therefore, the RF equivalent impedances at frequency $(\omega_P + 2\omega_{IF1})$ can be obtained as

$$Z_{gRF}(\omega_P + 2\omega_{IF1}) = Z_v(\omega_P + 2\omega_{IF1})$$
$$+ \frac{|S_{1,1}|^2}{(\omega_P + 2\omega_{IF1})\omega_{IF1}[Z_v(\omega_{IF}) + Z_{if}(\omega_{IF})]}$$
(31)

Thus, the output current at this frequency can be expressed with

$$I_{2sB} = \frac{V_{2sB}}{Z_{gRF}(\omega_P + 2\omega_{IF1}) + Z_{rf}(\omega_P + 2\omega_{IF1})}.$$
(32)

C. THIRD-ORDER SMALL-SIGNAL EQUIVALENCE AND IIP$_3$

The process to find IIP_3 is executed in the same manner as discussed in Section IV-B. First, the 3rd-order nonlinear voltage v_{3s} needs to be identified and have its power evaluated. Then, referring to the Thevenin equivalent for the 3rd-order equivalent parametric upconverter circuit shown in Fig. 7, the equivalent RF impedance will be calculated. At the end, the output power at frequency $[\omega_P + (2\omega_{IF1} - \omega_{IF2})]$ can be obtained.

As already explained in Section III, the 3rd-order nonlinear voltage derives from two different mixing mechanisms: *mechanism I* – the second-order interaction and *mechanism II* – the first-order direct mixture.

The 2nd-order currents that mediate *mechanism I*, I_{2sA} and I_{2sB}, were derived in Section IV-B. In analogy to our earlier methods, the contribution of these terms to our 3rd-order nonlinear voltage calculation is formalized by their inclusion in (16b). In particular, the 3rd-order nonlinear voltage indicative of *mechanism I* is expressed by again substituting the Fourier series equivalents, this time for $s_2(t)$, $i_1(t)$, and $i_2(t)$ into the first term to the right of the equals in (16b)

$$V_{3s,I}$$
$$= 2 \cdot \frac{1}{4}$$
$$\cdot \left\{ \sum_{k=-1}^{1} \sum_{m=-1}^{1} \sum_{n=-1}^{1} \left[\frac{S_{2,k} \cdot I_{m,2sA} \cdot I_{n,1}}{-[m\omega_P + (\omega_{IF1} - \omega_{IF2})](n\omega_P + \omega_{IF1})} \right. \right.$$
$$\left. \left. + \frac{S_{2,k} \cdot I_{m,2sB} \cdot I_{n,-2}}{-(m\omega_P + 2\omega_{IF1})(n\omega_P - \omega_{IF2})} \right] \right.$$
$$\left. \cdot e^{j[(k+m+n)\omega_P + (2\omega_{IF1} - \omega_{IF2})]t} \right\}$$
(33)

where $I_{m,2sA}$ and $I_{m,2sB}$ refer to the m-th harmonic of the 2nd-order current at frequencies $[\omega_P + (\omega_{IF1} - \omega_{IF2})]$ and $(\omega_P + 2\omega_{IF1})$, respectively. $I_{m,\pm l}$, again, indicates the m-th harmonic of the 1st-order current relating to input tones $\pm \omega_{IFl}$.

Mechanism II, the generation of the 3rd-order mixing product by the direct mixture of 1st-order input signals, is analyzed by expressing $s_3(t)$ and $i_1(t)$ with their Fourier series equivalents in the second term of (16b) to give

$$V_{3s,II} = \frac{1}{4} \cdot \left\{ \sum_{k=-1}^{1} \sum_{m=-1}^{1} \sum_{n=-1}^{1} \sum_{p=-1}^{1} \right.$$
$$\frac{S_{3,k} \cdot I_{m,1} \cdot I_{n,1} \cdot I_{p,-2}}{-j(m\omega_P + \omega_{IF1})(n\omega_P + \omega_{IF1})(p\omega_P - \omega_{IF2})}$$
$$\left. \cdot e^{j[(k+m+n+p)\omega_P + (2\omega_{IF1} - \omega_{IF2})]t} \right\}$$
(34)

where $I_{m,\pm l}$ denotes the m-th harmonic of 1st-order current associating to input tones $\pm \omega_{IFl}$.

Again applying the same method to derive the Thevenin equivalent impedances as that employed in Section IV-B, the Thevenin equivalent RF impedances at the 3rd-order equivalent circuit in Fig. 7 are given by

$$Z_{gRF}(\omega_P + 2\omega_{IF1} - \omega_{IF2})$$
$$= Z_v(\omega_P + 2\omega_{IF1} - \omega_{IF2})$$
$$+ \frac{|S_{1,1}|^2}{(\omega_P + 2\omega_{IF1} - \omega_{IF2})\omega_{IF1}[Z_v(\omega_{IF}) + Z_{if}(\omega_{IF})]}$$
(35)

Finally, the total current through the load impedance, Z_{rf}, at the 3rd-order frequency $[\omega_P + (2\omega_{IF1} - \omega_{IF2})]$ assumes the form

$$I_3(\omega_P + 2\omega_{IF1} - \omega_{IF2})$$
$$= \frac{V_{3s,I} + V_{3s,II}}{Z_{gRF}(\omega_P + 2\omega_{IF1} - \omega_{IF2}) + Z_{rf}(\omega_P + 2\omega_{IF1} - \omega_{IF2})}$$
(36)

which results in the corresponding output power

$$P_{out}(\omega_P + 2\omega_{IF1} - \omega_{IF2})$$
$$= \frac{1}{2} |I_3(\omega_P + 2\omega_{IF1} - \omega_{IF2})|^2 \Re(Z_{rf}).$$
(37)

The necessary expressions for the circuit-based constituents of the linearity parameters, IIP_2 in (1a) and IIP_3 in (1b), are now derived.

The expressions obtained so far formalize design intuition. For instance, (20) highlights how increases in $S_{1,1}$, a term regulated by the PUMP power [80], boosts conversion gain. In concert however, (25) to (28) and (33) to (37) expose a more sophisticated relationship between $S_{1,1}$ and the output powers at 2nd- and 3rd-order intermodulation products (i.e. IM2 and IM3, respectively).

To better understand this association we next examine the relationships predicted by our derived expressions with the help of an example.

V. INFLUENCE OF PUMP FREQUENCY AND POWER ON UPCONVERTER OPERATION

In this section, we will discuss design trade-offs between the PUMP frequency relative to the output frequency, transducer gain, G_t, the power (conversion) gain, G_p, and IIP_2 and IIP_3. Besides linearity, G_t and G_p indicate how efficiently parametric circuits can transfer the available input power to the load (i.e. G_t) and how efficiently they can deliver the input power to the load (i.e. G_p). More detailed discussions on G_t can be found in [77].
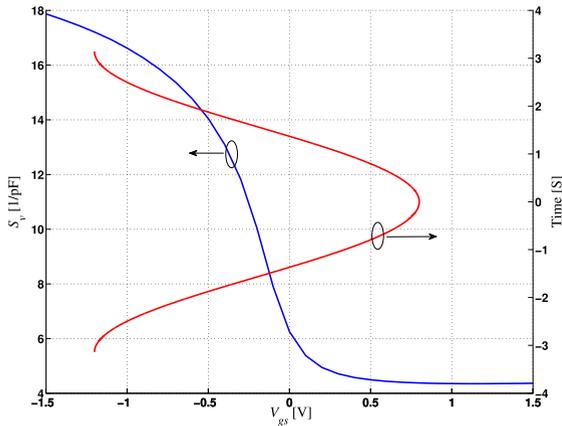
(a) Simulated S_v vs. biasing voltage (V_{gs}) across the varactor and the exciting biasing voltage in time domain with the assumption of peak-to-peak is 1 V while dc biasing offset is set to -0.1 V.
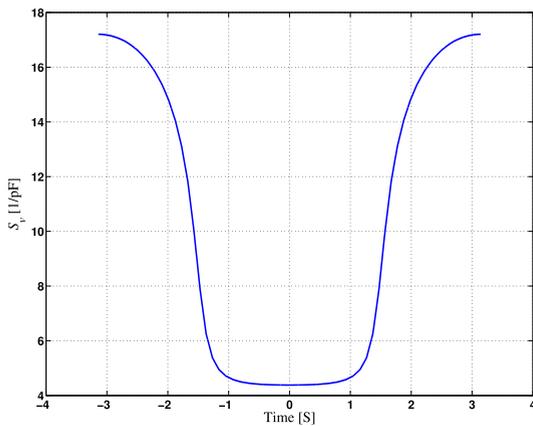
(b) Interpolated elastance in time domain for a given time-varying voltage biasing.

FIGURE 8. Illustration of proposed curve interpolation methodology to calculate Fourier coefficients of elastance.

We consider an RF upconverter employing an accumulation-mode MOS varactor (AMOSV). The AMOSV device model is chosen from a 0.13-μm CMOS technology and operated at -0.1-V dc bias. From simulation or measurement data, the AMOSV characteristics can be extracted as S-V curve for example in Fig. 8a. Then the time-varying voltage can be imposed on the curve to interpolate elastance in time domain, shown in Fig. 8b. Once elastance maps

in time, apply Fourier Transformation and Fouries coefficients (such as $S_{0,1}$, $S_{1,1}$, and other coefficients described in previous section) can be calculated. For the simplicity the angular speed for calculating the Fourier coefficients can be set to 1. This methodology can be applied to any monotonic relation of nonlinear voltage-controlled capacitor, resistor, and inductor. The reasonable accuracy between the analytic and measurement data can be achieved as the comparison results will be discussed in later section.

Following the methodology above, the chosen AMOSV exhibits the $|S_{1,1}|$ characteristics shown in Fig. 9 in relation to the PUMP power P_P delivered to it or the voltage amplitude V_m established across it by the PUMP. This device is further discussed in a parametric context in [78], [80].
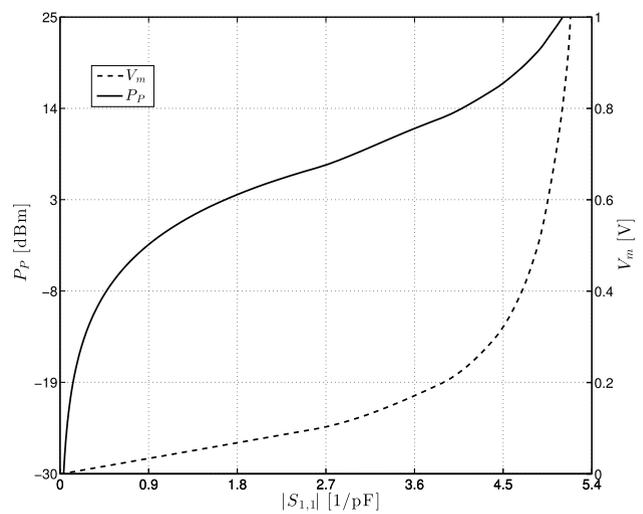

FIGURE 9. Simulated $|S_{1,1}|$ vs. the PUMP voltage across the varactor and the PUMP power delivered to it. The varactor model is from a 0.13-μm CMOS technology and operated at -0.1-V dc bias.

Fig. 9 indicates the expected increase in $|S_{1,1}|$ as a function of V_m. For V_m up to 0.3 V (i.e. delivered pump power around 31.6 mW) the $|S_{1,1}|$ increase is relatively rapid and saturates at higher PUMP settings, a consequence of the limited voltage range spanned by the AMOSV's accumulation and depletion regions.

These characteristics indicate that the voltage swings needed to establish near-maximum $|S_{1,1}|$ should be practical to achieve in the mm-wave range given an on-chip PUMP in a 0.13-μm CMOS technology. For example, as shown in the figure, $|S_{1,1}|$ saturates for $V_m \gtrsim 300$ mV, corresponding to a delivered PUMP power of 15-dBm. In practice much lower $|S_{1,1}|$ settings than this may satisfy a variety of applications. We elaborate on this below.

In the following, we discuss the USB and LSB operating modes of the parametric upconverter based on the varactor introduced above. In the calculations, it is assumed that the input source impedance Z_{if} and the output load impedance Z_{rf} in Fig. 6 are conjugate matched to the average varactor impedance Z_v at any frequency of interest. The RF frequency is set to 35 GHz and the frequency of the two-tone IF

input signals is centred at 1 GHz with a 1-MHz separation. In the following discussions, the available IF input power is fixed to −40 dBm. We begin with a treatment of upconverter behaviour in the USB mode followed by a discussion of the LSB upconverter.

A. USB UPCONVERTER

From the expressions previously derived, it is clear that $S_{1,1}$ plays a pivotal role in a parametric circuit's operation. It influences the equivalent impedances and effective voltages present at different mixing orders within the upconverter. Thus, the magnitude of $S_{1,1}$ needs to be determined before elaborating on the circuit performance characteristics. Fig. 9 shows a monotonic relationship between $|S_{1,1}|$ and P_P or V_m. In other words, once the PUMP power delivered to varactor or the voltage magnitude established across it by the PUMP are identified the $|S_{1,1}|$ can be determined accordingly. Therefore, in the following we will discuss the impact of P_P on the gain and linearity of the USB upconverter.
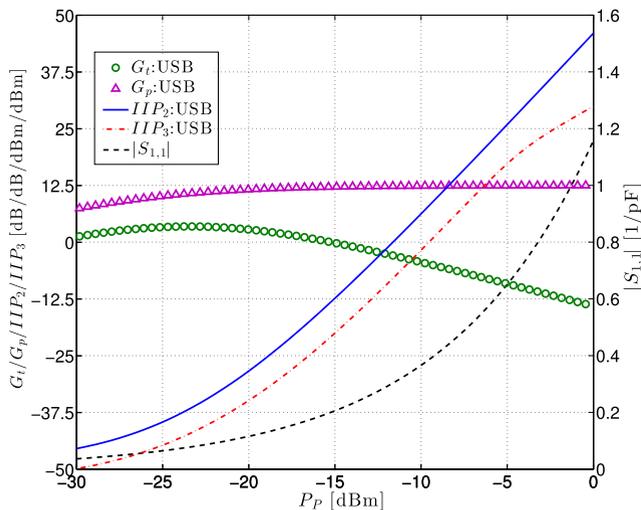

FIGURE 10. The calculated G_t, G_p, IIP_2, IIP_3 and simulated $|S_{1,1}|$ vs. P_P at f_{RF} = 35 GHz and f_{IF} = 1 GHz with $f_{spacing}$ = 1 MHz in USB-mode.

Figs. 10 and 11 detail G_t, G_p, IIP_2, IIP_3, and the power terms in the USB upconverter as a function of P_P. As implied by (19b) and (21b) and also noted in [77], a power match is possible in a USB-mode upconverter. Corresponding to this setting, $G_{t:USB}$, in Fig. 10, peaks at 3.52 dB when $P_P = -23.3$ dBm. At this point, the delivered output power $P_{out,1st:USB}$ also peaks, as confirmed in Fig. 11. Away from this optimal point, given mismatches at its source and load impedances (Z_{if} and Z_{rf}, respectively), $G_{t:USB}$ drops as expected.

As P_P increases, the Thevenin equivalent input impedance at ω_{IF}, $Z_{gIF,USB}$ in (19b), and the Thevenin equivalent output impedance at ω_{RF}, $Z_{gRF,USB}$ in (21b), both increase, reducing the power transfer efficiency and resulting in a drop in $G_{t:USB}$ as presented in Fig. 10.

On the other hand, increasing P_P boosts the amount of power transferred from the input to the load, which is
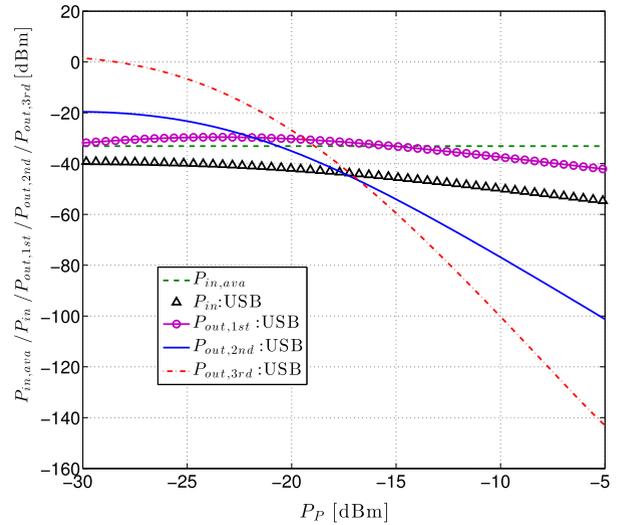

FIGURE 11. Calculated $P_{in,ava}$, P_{in}, fundamental output power $P_{out,1st:USB}$, 2nd-order intermodulation output power $P_{out,2nd:USB}$, 3rd-order intermodulation output power $P_{out,3rd:USB}$ vs. P_P region in USB-mode.

described by the operating power gain $G_{p:USB}$ in Fig. 10. As shown therein, $G_{p:USB}$ saturates at a value of 12.5 dB. Compared to the ideal scenario (i.e. a lossless varactor) the Manley-Rowe relations in [4] predict a maximum operating power gain of 15.5 dB for such a USB scenario. As they account for non-ideal varactor behaviour, our expressions predict about a 3-dB lower power gain; a result of pump power dissipation in the varactor before translation to ω_{RF}.

It is obvious that IIP_2 and IIP_3 both improve as P_P is increased. These improvements derive from the fact that the degradations in $P_{out,2nd:USB}$ and $P_{out,3rd:USB}$ with respect to P_P are two- and three-time faster than $P_{out,1st:USB}$, respectively [70].[1] A verification in Fig. 11 shows how these output power terms, $P_{out,1st:USB}$, $P_{out,2nd:USB}$ and $P_{out,3rd:USB}$, decrease at different rates. To be noted, $P_{out,1st:USB}$, $P_{out,2nd:USB}$, and $P_{out,3rd:USB}$ do not reach their optimal values simultaneously for their optimal impedances are different at their respective frequencies.

B. LSB UPCONVERTER

As captured by (19a) and (21a), in LSB mode the resistive components of $Z_{gIF,LSB}$ and $Z_{gRF,LSB}$ may be positive, zero, or negative depending on $|S_{1,1}|$. Therefore, this upconverter possesses both stable and unstable operating regimes. Consequently such an upconverter can deliver a broader range of output power than its USB counterpart, but at the cost of requiring more complicated operational considerations.

Fig. 12 shows the LSB upconverter's predicted $G_{t:LSB}$, $G_{p:LSB}$, IIP_2, and IIP_3 as a function of the PUMP power. In the figure, a sharp peak in the LSB upconverter's transducer power gain, $G_{t:LSB}$ (at $P_P = -23.3$ dBm) is exhibited.

---

[1]This is due to the square and cubic power index in $P_{out,2nd:USB}$ and $P_{out,3rd:USB}$ (in dBm scales these power indexes translate to multiplier factors).
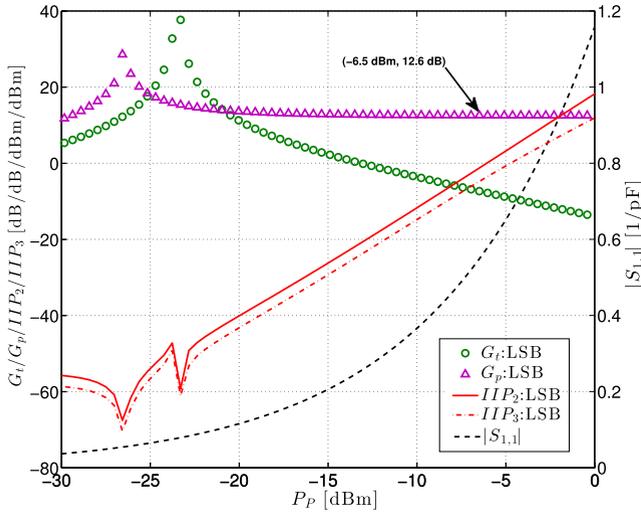
FIGURE 12. Calculated G_t, G_p, IIP_2, IIP_3 and simulated $|S_{1,1}|$ vs. P_P at $f_{RF} = 35$ GHz and $f_{IF} = 1$ GHz with $f_{spacing} = 1$ MHz in LSB mode.

FIGURE 13. Calculated $P_{in,ava}$, P_{in}, fundamental output power $P_{out,1st:LSB}$, 2nd-order intermodulation output power $P_{out,2nd:LSB}$, 3rd-order intermodulation output power $P_{out,3rd:LSB}$.

With reference to (19a) and (21a), at this P_P level, the net resistances in the IF and RF paths in Fig. 6 are null. Thus, the peak is indicative of the LSB upconverter's transition into an unstable region where the net resistance in the circuit is negative.

Mathematically speaking, at this null net resistance point, the upconverter could deliver infinite power to the load. In practice, an oscillatory behaviour, controllable via P_P, will arise, where the frequency of oscillation is ultimately dependent on the combination of ω_{IF}, ω_P, and ω_{RF} used. Such behaviour still enables the parametric circuit to realize a useful function such as injection-locked oscillation, a phenomenon reported in [81].

At low P_P ($P_P < -23.3$ dBm), the net resistances in the IF and RF paths are positive and the circuit operates in a stable region. In this stable region, both the transducer gain, $G_{t:LSB}$ and power gain, $G_{p:LSB}$ rise quickly towards a sharp peak (at P_P=-26 and -23.3 dBm, respectively for this example) as P_P increases. This rise is caused by the resistance drops in the upconverter's IF and RF paths when approaching $P_P = -26$ dBm from below.

With P_P set above -23.3 dBm, the upconverter exhibits a net negative input resistance and thus reflects its input signal back to the source [77], [82]. Therefore, under such P_P settings, the parametric circuit effectively serves as a straight (reflection) amplifier rather than a frequency converter [8], [69].

Fig. 12 also shows that the peaks of $G_{t:LSB}$ and $G_{p:LSB}$ occur at different ordinates. This is simply a result of the alternate gain definitions. That is, $G_{p:LSB}$ accounts for the input power while $G_{t:LSB}$ is based on the available input power. As a result, different source resistance settings are employed by the different definitions therefore shifting the P_P level at which the circuit's negative input resistance causes a shift in its region of operation.

With increases in P_P in the LSB's stable region, the $P_{out,1st:LSB}$ harmonic rises (Fig. 13) due to a drop in Z_{gRF}
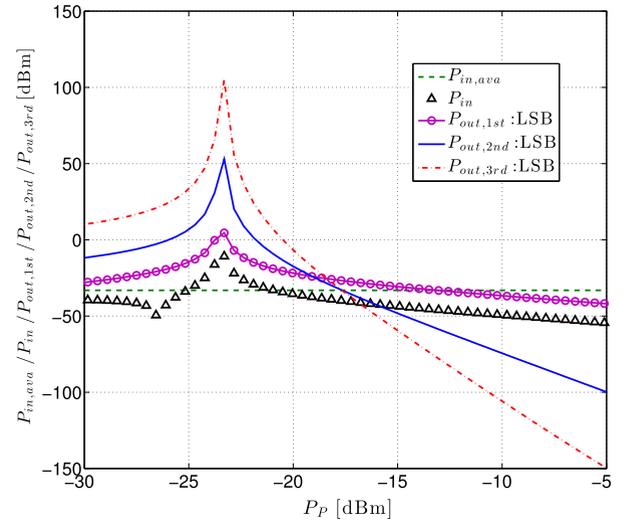
(leading to a reduction in (23)'s denominator). Unfortunately, the 2nd- and 3rd- harmonics increase at an even faster rate leading to the dips in IIP_2 and IIP_3 observable in Fig. 12.

As noted above, in Fig. 12, at $P_P > -23.3$ dBm, the LSB upconverter's net resistances becomes negative. The power gain equations in Appendix VII indicate that at high $|S_{1,1}|$ both LSB and USB G_p becomes independent on $|S_{1,1}|$ and becomes associated only with the ratio of input and output frequencies as well as the varactor's internal loss and load impedances. Therefore, in Fig. 12, the power gain, $G_{p:LSB}$, decreases, eventually settling to 12.6 dB at $P_P \geq -6.5$ dBm.

It is also noticeable in Fig. 12 that both IIP_2 and IIP_3 steadily improve for $P_P > -23.3$ dBm due to the rapid drops in $P_{out,2nd:LSB}$ and $P_{out,3rd:LSB}$. This resembles the enhancements of IIP_2 and IIP_3 exhibited in USB mode at high P_P levels as discussed previously in Section V-A. However, for the LSB in this region, the parametric circuit only exhibits negative resistances and, for robust design needs, is typically avoided.

To summarize, the USB mode parametric upconverter only contains positive resistance and thus is stable. With increases in its PUMP power the USB's power gain saturates close to the Manley-Rowe estimate while the IIP_2 and IIP_3 improve. On the other hand, the LSB mode parametric upconverter demonstrates an excellent gain at low P_P due to its introduction of negative resistance components. Unfortunately, the linearity of the circuit exhibits inferiority and the circuit has a greater potential to be unstable. Similar to the USB upconverter, the IIP_2 and IIP_3 in LSB mode can also be enhanced by using higher P_P albeit in the presence of negative resistances that may cause instability.

Therefore, a trade-off exists: in USB mode, superior linearity can be achieved with limited power gain (less than Manley-Rowe's prediction due to the internal loss of the varactor); alternatively the LSB parametric upconverter
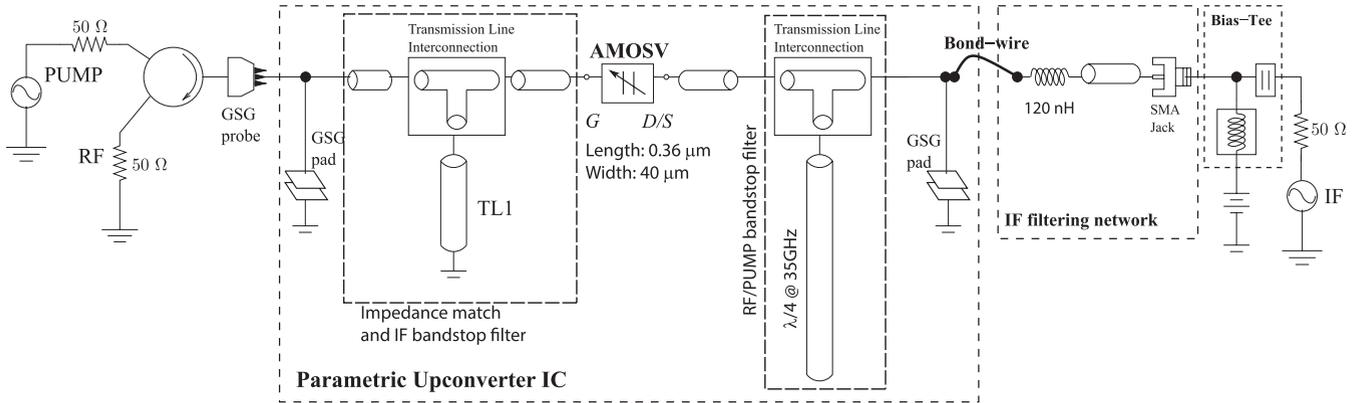
FIGURE 14. Schematic of the implemented upconverter.

possesses excellent power gain at the cost of poor linearity. To take advantage of both modes, with a simple shift in the PUMP frequency, ω_P, a circuit (e.g. like the one discussed in Section VI) in LSB mode can be conveniently configured to USB mode operation and thus guaranteed stability. Of course, the availability of negative resistance in certain LSB regions of operation offers the potential for superior gain if P_P is carefully set and controlled. In integrated contexts, where on-chip signal monitoring and control is relatively cheap [77], [81], [82] such scenarios become realistic. Hence, with an appropriate change to ω_P, the circuit can be switched to a reliable mode of high-gain operation. Thus, the parametric circuit has the potential to be configured for high-gain or high-linearity for potentially satisfying different application requirements

In this section, a quantitive measure of the linearity of the parametric upconverter has been formulated and an example of an ideal parametric upconverter has also been discussed. In the next section, we utilize the calculations developed in Section IV to predict the linearity of a parametric upconverter implemented in 0.13-μm CMOS technology and then compare the results to simulated and measured data to verify the approach.

VI. IC IMPLEMENTATION AND MEASUREMENTS
Having determined output powers at the fundamental tones and higher harmonics, the linearity of a parametric upconverter can be analyzed as discussed in Section IV. Presently, our theoretical approximations are compared to simulated and measured data. Specifically, a 36-GHz integrated upconverter design previously discussed in [46] is compared. This upconverter, which was previously designed specifically to study operation of parametric frequency converters and to experimentally demonstrate frequency upconversion in a silicon technology, translates a 1-GHz IF signal to a 36-GHz RF signal by using an Agilent E8247C signal generator as a PUMP operating at 35 GHz for USB mode and 37 GHz for LSB mode, respectively.

The design schematic and micrograph of the IC are presented in Fig. 14 and Fig. 15, respectively. As shown,
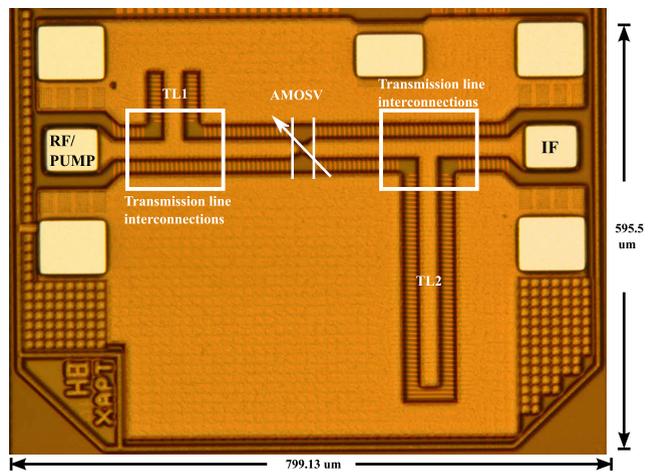

FIGURE 15. Micrograph of the parametric 36-GHz 0.13-μm CMOS upconverter.

in Fig. 14 the IF signal is delivered to the upconverter through an off-chip filtering network via a bond-wire. Then it travels through the varactor from the G node to the D/S node at which point the IF signal is grounded by a shorted quarter-wavelength transmission line, TL1, that completes the IF loop (spanning the IF source and TL1) across the varactor. Simultaneously, TL1 prevents the PUMP signal from being shunted to ground before node G and thus allowing it to excite the AMOSV mixing element.

The PUMP signal loop, which is introduced via a ground-signal-ground (GSG) probe, is completed at the D/S node by the unterminated 3/4-wavelength transmission line, TL2. The IF signal is at too low a frequency to be affected by TL2's signal propagation characteristics.

The RF signal established across the AMOSV due to IF and PUMP mixing is tapped out of the IC through the aforementioned GSG probe and directed to an RF terminator via a circulator element. Since the frequencies of the RF and PUMP signals are in proximity, the bandstop and bandpass properties of TL1 and TL2 respectively also apply to the RF signal. As a result, the signal loops for all three frequencies of interest are completed.

The Agilent ADS software package [83] is used to carry out the upconverter circuit simulations. Foundry-provided 0.13-μm CMOS AMOSV models are used. For improved simulation accuracy, the on-chip GSG pads and transmission lines shown in Fig. 14 are simulated in HFSS [84] and their extracted S-parameters imported into the ADS simulations. A similar procedure is followed for the off-chip components. Mainly, the S-parameters of the external RF cables, circulator, bias-Tee's, and IF filtering network are used in the simulations for better prediction.

The measurements presented in this paper were only configured for investigating the linearity of the varactor-based CMOS parametric upconverter and verifying the theory discussed in Section IV. Thus, achieving an optimal conversion gain is not the objective of this paper. Further, the input and output frequencies are 0.5 GHz and 35.5 GHz, respectively, in [46] while in this paper 1 GHz and 36 GHz are selected. This frequency selection lowers the theoretical maximum conversion gain by about 3 dB according to the Manley-Rowe energy relationship [4]. Therefore, the measured conversion gain presented in this paper is lower than the one reported in [46].
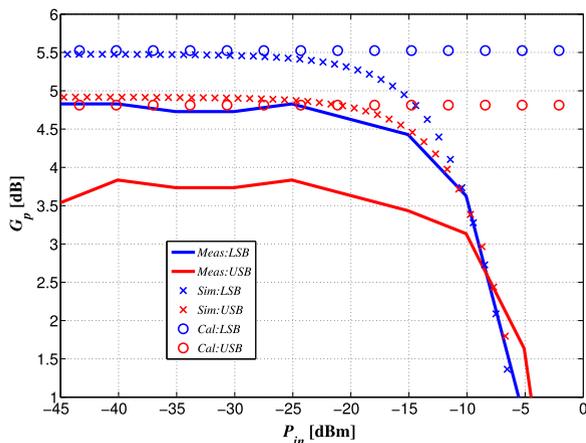

FIGURE 16. Measurement, simulation, and theoretical calculation result comparison of the conversion gain for the LSB and USB upconverters.

Firstly, Fig. 16 compares the LSB and USB upconverter conversion gain between measurements, simulated data, and theoretical calculations. In the figure, between measurements and simulations, there is $\sim$0.5-dB difference for the LSB configuration and <1.5-dB discrepancy for the USB. The offsets are due to errors in de-embedding, the external interfaces (such as RF cables, connectors, RF probes and so on) from the measurement data, and the 30-GHz limitation of the chosen CMOS process' available circuit models [85]. In particular, the evaluation of path loss for de-embedding purposes relies on power gain calculations [86]; as a result, interface mismatches are accounted for by estimating the port impedances of the equipment as well as the input and output impedances of the device-under-test. To simplify the measurement setup, these were estimated using S-parameter measurements with the PUMP disengaged, a technique

that does not capture the full large-signal characteristics at the mixer ports and hence introduces some error. The 0.5- and 1.5-dB differences between the measured, calculated, and simulated conversion gains for LSB and USB, respectively, shown in Fig. 16 indicate that these de-embedded approximations are reasonable.

On the other hand, the difference between simulations and theoretical calculations originates from the accuracy of evaluations of the elastance Fourier series coefficients. The theoretical estimation of conversion gain shown in Fig. 16 is a first-order approximation. Also, assumption 4) in Section II of weakly nonlinear operation, prompted our use of a small-signal analysis. Thus, the theoretical algorithm presented in Section IV does not model the gain compression phenomenon and only considers the small-signal behaviour of the circuit as exhibited by the constant calculated LSB and USB conversion gain in Fig. 16.
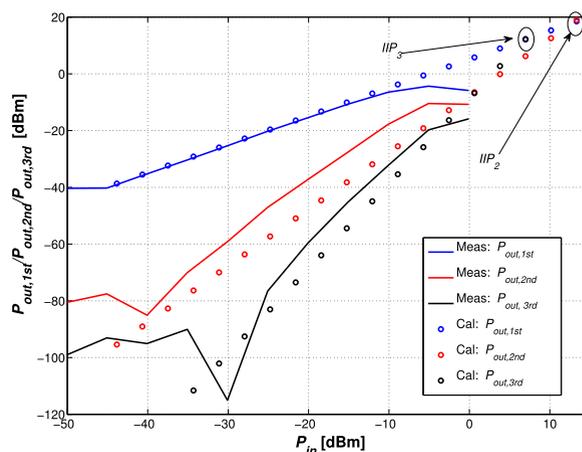

FIGURE 17. Measured and theoretical output powers at the fundamental, 2nd-order, and 3rd-order mixing products with $k = \pm 1$ and 0.

TABLE 1. Measured and calculated IIP_2 and IIP_3 comparison.

	Meas.	**Cal.** (1st-order)	**Cal.** (2nd-order)
IIP_2 [dBm]	1.7	14.3	3
IIP_3 [dBm]	2	6.1	4.9

A comparison of the output fundamental, 2nd-, and 3rd-order powers observed from measurements and predicted using our theoretical calculations can be found in Fig. 17. Table 1 summarizes the measured IIP_2 and IIP_3 in its second column while the 1st-order calculated values are presented in the third column. The 1st-order model results in approximately a 12.1-dB difference between measured IIP_2 and theoretical predictions while, for the IIP_3, there is about a 4.1-dB offset. These discrepancies mainly come from the fact that to simplify the theoretical analysis we initially only consider the first harmonic of the Fourier series coefficients of $s_1(t)$, $s_2(t)$ and $s_3(t)$. This approximation implies that only a single-sideband current would be circulated in the circuit. That is, the current is at either $\omega_P + \omega_{IF}$ or $\omega_P - \omega_{IF}$ for $P_{out,1st}$ and either $\omega_P + (\omega_{IF1} - \omega_{IF2})$ or $\omega_P - (\omega_{IF1} - \omega_{IF2})$ for IM2 as

well as either $\omega_P + (2\omega_{IF1} - \omega_{IF2})$ or $\omega_P - (2\omega_{IF1} - \omega_{IF2})$ for IM3. However, according to the output filter design [46], the currents at both frequency sidebands exist and exert influence on the output power. Thus, the nonlinear effects are underestimated. This can be remedied by extending the prediction to include 2nd-order effects by setting k to ± 2, ± 1 and 0. Fig. 18 and the fourth column of Table 1 show that after increasing the order of the harmonics included in the theoretical calculation, the disagreement of the curves for both 2nd- and 3rd-order output power predictions and measurement data has improved to 1.3 dB and 2.9 dB for IIP_2 and IIP_3, respectively.

Fig. 17 shows that our theoretical calculations can adequately predict the fundamental, 2nd-, and 3rd-order output powers with a 1st-order approximation even though IIP_2 and IIP_3 projections are removed from the measurement data. Certainly by considering more harmonics the accuracy of the predictions improves as seen in Fig. 18. Unfortunately, accounting for more harmonics increases the complexity of the expressions exponentially and it may be tricky to gain clear design insights. Thus, at an early stage in the design phase, the first-order can be seen as a reasonable tool to gain a quick design intuition.
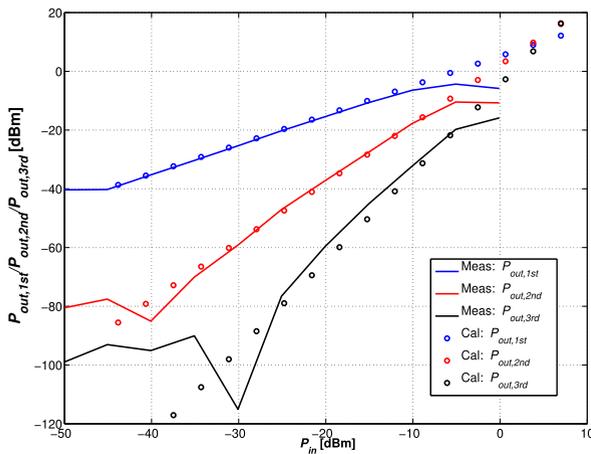

FIGURE 18. Measured and theoretical output powers at the fundamental, 2nd-order, and 3rd-order mixing products with $k = \pm 2$, ± 1 and 0.

VII. CONCLUSION

This paper demonstrates the application of a conversion matrix analysis to a CMOS parametric upconverter in the millimetre frequency range. It shows no more than a 1.5-dB conversion gain difference for both LSB and USB upconverter configurations. Also, with a second-order linearity approximation about 1.3-dB and 2.9-dB offsets for IIP_2 and IIP_3 estimation, respectively, between measurement and theoretical predictions are present. The similarity in the comparison of results between the theoretical analysis, simulations, and measurements indicates that this proposed curve interpolation and linearity analysis is a viable tool for analyzing the linearity of the varactor-based CMOS parametric

mixer design intended for the millimeter-wave region. This approach could be used to identify the contributors to the linearity characteristics of millimeter-wave parametric mixers so as to optimize them for application specifications. This paper also demonstrates the accuracy improvement obtained by including higher-order effects into the theoretical linearity prediction. Naturally, such including such terms increases the complexity of the calculation accordingly. Therefore, at an early stage of the design process, one can implement the first-order linearity approximation for a quick evaluation and determine a matching strategy. Following design iterations can evaluate the circuit linearity more accurately and subsequently gain deeper insights with higher-order analyses.

APPENDIX
SMALL-SIGNAL POWER GAIN EQUATIONS FOR PARAMETRIC UPCONVERTERS

In this appendix, the small-signal power gain equations for LSB and USB parametric upconverters are derived. The schematic diagram for this derivation is shown in Fig. 19. In the figure, the PUMP signal path has been omitted since the PUMP signal effects are captured by the small-signal Z-parameter representatives. Depending on which mode the upconverter is made to assume (i.e. USB or LSB), the Z-parameters differ and their matrices can be referred to in Eqn. (18).
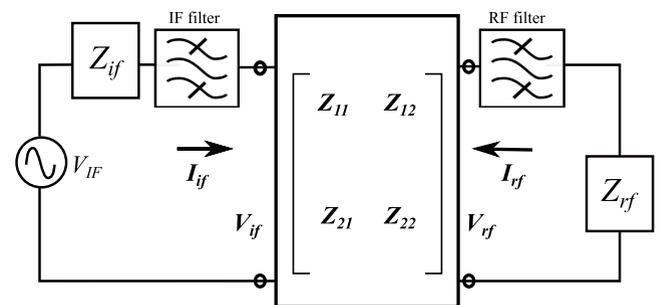

FIGURE 19. Small-signal representative of the parametric upconverter for power gain derivations. The filters are ideal that pass the frequencies of interest and block the unwanted ones.

According to [86], the power gain is defined as the ratio of delivered output power to the input power, that is

$$G_p = \frac{P_{out}}{P_{in}} \qquad (38)$$

where referring to Fig. 19 P_{out} can be calculated as

$$P_{out} = \frac{|V_{rf}|^2}{2\Re\{Z_{rf}\}} \qquad (39)$$

and P_{in} can be expressed as

$$P_{out} = \frac{|V_{if}|^2}{2\Re\{Z_{in}\}} \qquad (40)$$

where Z_{in} denotes the input impedance seen from the IF to the RF path.

This input impedance can be further calculated in term of Z-parameters as

$$Z_{in} = Z_{11} - \frac{Z_{12}Z_{21}}{Z_{22} + Z_{rf}}. \qquad (41)$$

Applying KVL and replacing P_{out} and P_{in} into (38), then we can reach the small-signal power gains expressions for USB and LSB as

$$G_{p:USB} = \frac{\frac{|S_{1,1}|^2}{\omega_{IF}^2}(R_{rf}^2 + |X_{rf}|^2)}{\left|(R_s + \frac{S_{1,0}}{j\omega_{RF}}(R_s + R_{rf}) + \frac{|S_{1,1}|^2}{(\omega_{IF}\omega_{RF})}\right|^2} \times \frac{R_s + |S_{1,1}|^2/[\omega_{IF}\omega_{RF}(R_s + R_{rf})]}{R_{rf}} \qquad (42)$$

$$G_{p:LSB} = \frac{\frac{|S_{1,1}|^2}{\omega_{IF}^2}(R_{rf}^2 + |X_{rf}|^2)}{\left|(R_s + \frac{S_{1,0}}{j\omega_{RF}}(R_s + R_{rf}) - \frac{|S_{1,1}|^2}{(\omega_{IF}\omega_{RF})}\right|^2} \times \frac{R_s - |S_{1,1}|^2/[\omega_{IF}\omega_{RF}(R_s + R_{rf})]}{R_{rf}} \qquad (43)$$

where R_{rf} and X_{rf} are real and imaginary parts of Z_{rf}.

If $S_{1,1}$ increases significantly and assume $X_{rf} = S_{1,0}/j\omega_{RF}$ for USB and $X_{rf} = -S_{1,0}/j\omega_{RF}$ for LSB, then the equations above can be re-written as

$$\lim_{|S_{1,1}| \to \infty} G_{p:USB} = \frac{\omega_{RF}}{\omega_{IF}} \frac{R_{rf}[(R_{rf})^2 + |X_{rf}|^2]}{R_s + R_{rf}} \qquad (44)$$

$$\lim_{|S_{1,1}| \to \infty} G_{p:LSB} = -\frac{\omega_{RF}}{\omega_{IF}} \frac{R_{rf}[(R_{rf})^2 + |X_{rf}|^2]}{R_s + R_{rf}}. \qquad (45)$$

REFERENCES

[1] W. Dornig, "Der Hochfrequenz-Maschinen-sender (400KM) Nauen," in *Telefunken-Zeitung*. Berlin, Germany: Gesellschaft für drahtlose Telegraphie, Aug. 1919, pp. 65–74.

[2] H. Q. North, "Properties of welded contact germanium rectifiers," *J. Appl. Phys.*, vol. 17, no. 11, pp. 912–923, Nov. 1946.

[3] H. C. Torrey and C. A. Whitmer, *Crystal Rectifiers* (MIT Radiation Lab Series), vol. 15. London, U.K.: McGraw-Hill, 1948.

[4] J. M. Manley and H. E. Rowe, "Some general properties of nonlinear elements-part i. general energy relations," *Proc. IRE*, vol. 44, no. 7, pp. 904–913, Jul. 1956.

[5] H. Suhl, "Proposal for a ferromagnetic amplifier in the microwave range," *Phys. Rev.*, vol. 106, pp. 384–385, Apr. 1957.

[6] M. T. Weiss, "A solid-state microwave amplifier and oscillator using ferrites," *Phys. Rev.*, vol. 107, pp. 384–385, Jul. 1957.

[7] A. E. Bakanowski, N. G. Cranna, and J. A. Uhlir, "Diffused silicon non-linear capacitors," *IRE Trans. Electron Devices*, vol. 6, no. 4, pp. 384–390, Oct. 1959.

[8] G. L. Matthaei, "A study of the optimum design of wide-band parametric amplifiers and up-converters," *IRE Trans. Microw. Theory Tech.*, vol. 9, no. 1, pp. 23–38, Jan. 1961.

[9] W. W. Mumford, "Some notes on the history of parametric transducers," *Proc. IRE*, vol. 48, no. 5, pp. 848–853, May 1960.

[10] L. A. Blackwell and K. L. Kotzebue, *Semiconductor-Diode Parametric Amplifiers*. Englewood Cliffs, NJ, USA: Prentice-Hall, 1961.

[11] I. Mehdi, P. H. Siegel, D. A. Humphrey, T. H. Lee, R. J. Dengler, J. E. Oswald, A. Pease, R. Lin, H. Eisele, R. Zimmermann, and N. Erickson, "An all solid-state 640 GHz subharmonic mixer," in *IEEE MTT-S Int. Microw. Symp. Dig.*, vol. 2, Jun. 1998, pp. 403–406.

[12] J. Bruston, R. P. Smith, S. C. Martin, D. Humphrey, A. Pease, and P. H. Siegel, "Progress towards the realization of MMIC technology at submillimeter wavelengths: A frequency multiplier to 320 GHz," in *IEEE MTT-S Int. Microw. Symp. Dig.*, vol. 2, Jun. 1998, pp. 399–402.

[13] J. E. Oswald, T. Koch, I. Mehdi, A. Pease, R. J. Dengler, T. H. Lee, D. A. Humphrey, M. Kim, P. H. Siegel, M. A. Frerking, and N. R. Erickson, "Planar diode solid-state receiver for 557 GHz with state-of-the-art performance," *IEEE Microw. Guided Wave Lett.*, vol. 8, no. 6, pp. 232–234, Jun. 1998.

[14] I. Mehdi, S. M. Marazita, D. A. Humphrey, T.-H. Lee, R. J. Dengler, J. E. Oswald, A. J. Pease, S. C. Martin, W. L. Bishop, T. W. Crowe, and P. H. Siegel, "Improved 240-GHz subharmonically pumped planar Schottky diode mixers for space-borne applications," *IEEE Trans. Microw. Theory Techn.*, vol. 46, no. 12, pp. 2036–2042, Dec. 1998.

[15] P. H. Siegel, R. P. Smith, M. C. Graidis, and S. C. Martin, "2.5-THz GaAs monolithic membrane-diode mixer," *IEEE Trans. Microw. Theory Techn.*, vol. 47, no. 5, pp. 596–604, May 1999.

[16] F. Maiwald, S. Martin, J. Bruston, A. Maestrini, T. Crawford, and P. H. Siegel, "2.7 THz waveguide tripler using monolithic membrane diodes," in *IEEE MTT-S Int. Microw. Symp. Dig.*, vol. 3, May 2001, pp. 1637–1640.

[17] I. Mehdi and P. Siegel, "THz semiconductor-based front-end receiver technology for space applications," in *Proc. IEEE Radio Wireless Conf.*, Sep. 2004, pp. 127–130.

[18] J. S. Ward, G. Chattopadhyay, J. Gill, H. Javadi, C. Lee, R. Lin, A. Maestrini, F. Maiwald, I. Mehdi, E. Schlecht, and P. Siegel, "Tunable broadband frequency-multiplied terahertz sources," in *Proc. 33rd Int. Conf. Infr., Millim. THz Waves*, Sep. 2008, pp. 1–3.

[19] T. Bryllert, K. B. Cooper, R. J. Dengler, N. Llombart, G. Chattopadhyay, E. Schlecht, J. Gill, C. Lee, A. Skalare, I. Mehdi, and P. H. Siegel, "A 600 GHz imaging radar for concealed objects detection," in *Proc. IEEE Radar Conf.*, May 2009, pp. 1–3.

[20] J. V. Siles, G. Chattopadhyay, E. Schlecht, C. Lee, R. Lin, J. Gill, J. Ward, C. Jung, I. Mehdi, P. Siegel, and A. Maestrini, "Next generation solid-state broadband frequency-multiplied terahertz sources," in *Proc. IEEE Int. Symp. Antennas Propag.*, Jul. 2012, pp. 1–2.

[21] T. W. Crowe and R. J. Mattauch, "GaAs Schottky barrier diodes for high sensitivity millimeter and submillimeter wavelength receivers," in *IEEE MTT-S Int. Microw. Symp. Dig.*, vol. 2, May 1987, pp. 753–756.

[22] T. W. Crowe, R. J. Mattauch, H. P. Roser, W. L. Bishop, W. C. B. Peatman, and X. Liu, "GaAs Schottky diodes for THz mixing applications," *Proc. IEEE*, vol. 80, no. 11, pp. 1827–1841, Nov. 1992.

[23] S. S. Gearhart, J. Hesler, W. L. Bishop, T. W. Crowe, and G. M. Rebeiz, "A wide-band 760-GHz planar integrated Schottky receiver," *IEEE Microw. Guided Wave Lett.*, vol. 3, no. 7, pp. 205–207, Jul. 1993.

[24] K. Hui, J. L. Hesler, D. S. Kurtz, W. L. Bishop, and T. W. Crowe, "A micromachined 585 GHz Schottky mixer," *IEEE Microw. Guided Wave Lett.*, vol. 10, no. 9, pp. 374–376, Sep. 2000.

[25] D. S. Kurtz, J. L. Hesler, T. W. Crowe, and R. M. Weikle, "Submillimeter-wave sideband generation using varactor Schottky diodes," *IEEE Trans. Microw. Theory Techn.*, vol. 50, no. 11, pp. 2610–2617, Nov. 2002.

[26] Q. Xiao, J. L. Hesler, Y. Duan, T. W. Crowe, and R. M. Weikle, "A 300-GHz heterostructure barrier varactor (HBV) frequency septupler," in *Proc. Joint 30th Int. Conf. Infr. Millim. Waves 13th Int. Conf. THz Electron.*, vol. 1, Sep. 2005, pp. 80–81.

[27] H. Xu, Y. Duan, J. L. Hesler, T. W. Crowe, and R. W. Weikle, "Subharmonically pumped millimeter-wave upconverters based on heterostructure barrier varactors," *IEEE Trans. Microw. Theory Techn.*, vol. 54, no. 10, pp. 3648–3653, Oct. 2006.

[28] J. L. Hesler, K. Hui, and T. W. Crowe, "A broadband 440–590 GHz receiver," in *Proc. 36th Int. Conf. Infr., Millim. THz Waves (IRMMW-THz)*, Oct. 2011, pp. 1–3.

[29] T. W. Crowe, D. W. Porterfield, and J. L. Hesler, "Multiplier-based sources of terahertz power," in *Proc. 33rd Int. Conf. Infr., Millim. THz Waves*, Sep. 2008, p. 1.

[30] J. L. Hesler, L. Liu, H. Xu, Y. Duan, and R. M. Weikle, "The development of quasi-optical thz detectors," in *Proc. 33rd Int. Conf. Infr., Millim. THz Waves*, Sep. 2008, pp. 1–2.

[31] J. Hesler, K. Hui, and T. Crowe, "Ultrafast millimeter-wave and THz envelope detectors for wireless communications," in *Proc. Int. Topical Meeting Microw. Photon. (MWP)*, Sep. 2012, pp. 93–94.

[32] K. K. O, "Sub-millimeter wave CMOS integrated circuits and systems," in *Proc. IEEE Int. Symp. Radio-Freq. Integr. Technol. (RFIT)*, Nov. 2011, pp. 1–8.

[33] R. Malik, A. Kumpera, M. Karlsson, and P. A. Andrekson, "Demonstration of ultra wideband phase-sensitive fiber optical parametric amplifier," *IEEE Photon. Technol. Lett.*, vol. 28, no. 2, pp. 175–177, Jan. 15, 2016.

[34] S. H. Wang and P. K. A. Wai, "Polarization pulling in fiber optical parametric amplifiers," in *Proc. 21st OptoElectronics Commun. Conf. (OECC) Held Jointly Int. Conf. Photon. Switching (PS)*, Jul. 2016, pp. 1–3.

[35] M. Jamshidifar, A. Vedadi, and M. E. Marhic, "Continuous-wave two-pump fiber optical parametric amplifier with 60 db gain," in *Proc. Conf. Lasers Electro-Opt. (CLEO)-Laser Sci. Photonic Appl.*, Jun. 2014, pp. 1–2.

[36] X. Wei, A. K. S. Lau, Y. Xu, C. Zhang, A. Mussot, A. Kudlinski, K. K. Tsia, and K. K. Y. Wong, "All-fiber optical parametric amplifier for life-science application," in *Proc. Conf. Lasers Electro-Opt. (CLEO)-Laser Sci. Photonic Appl.*, Jun. 2014, pp. 1–2.

[37] M. Jamshidifar, A. Vedadi, and M. E. Marhic, "Continuous-wave one-pump fiber optical parametric amplifier with 270 nm gain bandwidth," in *Proc. 35th Eur. Conf. Opt. Commun.*, Sep. 2009, pp. 1–2.

[38] Virginia Diodes Inc. *Dectectors*. Accessed: Oct. 28, 2016. [Online]. Available: http://www.vadiodes.com/index.php/en/products/detectors

[39] R. Han, Y. Zhang, Y. Kim, D. Y. Kim, H. Shichijo, E. Afshari, and K. K. O, "280 GHz and 860 GHz image sensors using Schottky-barrier diodes in $0.13\mu m$ digital CMOS," in *IEEE Int. Solid-State Circuits Conf. (ISSCC) Dig. Tech. Papers*, Feb. 2012, pp. 254–256.

[40] Z. Ahmad, M. Lee, and K. K. O, "1.4 THz, -13 dbm-EIRP frequency multiplier chain using symmetric- and asymmetric-CV varactors in 65 nm CMOS," in *IEEE Int. Solid-State Circuits Conf. (ISSCC) Dig. Tech. Papers*, Jan. 2016, pp. 350–351.

[41] Y. Zhang, R. Han, Y. Kim, D. Y. Kim, H. Shichijo, S. Sankaran, C. Mao, E. Seok, D. Shim, and K. K. O, "Schottky diodes in CMOS for terahertz circuits and systems," in *Proc. IEEE 13th Topical Meeting Silicon Monolithic Integr. Circuits RF Syst. (SiRF)*, Jan. 2013, pp. 24–26.

[42] V. P. Trivedi, J. P. John, K.-H. To, and W. M. Huang, "A novel integration of Si Schottky diode for mmWave CMOS, low-power SoCs, and more," *IEEE Electron Device Lett.*, vol. 32, no. 3, pp. 258–260, Mar. 2011.

[43] M. Matters, G. Gerini, and L. Tripodi. (Oct. 2010). *THz Imaging and Spectroscopy: The Next Wireless Wave*. Accessed: Oct. 28, 2016. [Online]. Available: https://static.tue.nl/fileadmin/content/faculteiten/ee/Onderzoek/Technologische_centra/Centre_for_Wireless_Technology/3_-_Giampiero_Gerini_-_Marion_Matters_-_THz.pdf

[44] Z. Zhao, J.-F. Bousquet, and S. Magierowski, "100 GHz parametric CMOS frequency doubler," *IEEE Microw. Wireless Compon. Lett.*, vol. 20, no. 12, pp. 690–692, Dec. 2010.

[45] Z. Zhao, J.-F. Bousquet, and S. Magierowski, "Parametric THz frequency multiplication using CMOS technology," in *Proc. 23rd Can. Conf. Electr. Comput. Eng. (CCECE)*, May 2010, pp. 1–5.

[46] Z. Zhao, S. Magierowski, and L. Belostotski, "35.5 GHz parametric CMOS upconverter," *IEEE Microw. Wireless Compon. Lett.*, vol. 22, no. 9, pp. 477–479, Sep. 2012.

[47] R. Han and E. Afshari, "A broadband 480-GHz passive frequency doubler in 65-nm bulk CMOS with 0.23 mW output power," in *Proc. IEEE Radio Freq. Integr. Circuits Symp. (RFIC)*, Jun. 2012, pp. 203–206.

[48] R. Han and E. Afshari, "A high-power broadband passive terahertz frequency doubler in CMOS," *IEEE Trans. Microw. Theory Techn.*, vol. 61, no. 3, pp. 1150–1160, Mar. 2013.

[49] M. Adnan and E. Afshari, "Efficient microwave and millimeter-wave frequency multipliers using nonlinear transmission lines in CMOS technology," *IEEE Trans. Microw. Theory Techn.*, vol. 63, no. 9, pp. 2889–2896, Sep. 2015.

[50] K. K. O, C. Cao, E.-Y. Seok, and S. Sankaran, "100-200 GHz CMOS signal sources and detectors," in *Proc. IEEE Compound Semiconductor Integr. Circuits Symp.*, Oct. 2007, pp. 1–4.

[51] C. Mao, C. Nallani, S. Sankaran, E. Seok, and K. K. O, "125-GHz diode frequency doubler in 0.13-um CMOS," *IEEE J. Solid-State Circuits*, vol. 44, no. 5, pp. 1531–1538, May 2009.

[52] D. Shim, C. Mao, R. Han, S. Sankaran, E. Seok, C. Cao, W. Knap, and K. K. O, "Paths to terahertz CMOS integrated circuits," in *Proc. IEEE Custom Integr. Circuits Conf.*, Sep. 2009, pp. 657–664.

[53] E. Seok, D. Shim, C. Mao, R. Han, S. Sankaran, C. Cao, W. Knap, and K. K. O, "Progress and challenges towards terahertz CMOS integrated circuits," *IEEE J. Solid-State Circuits*, vol. 45, no. 8, pp. 1554–1564, Aug. 2010.

[54] Z. Ahmad, I. Kim, and K. K. O, "0.39–0.45 THz symmetric MOS-varactor frequency tripler in 65-nm CMOS," in *Proc. IEEE Radio Freq. Integr. Circuits Symp. (RFIC)*, May 2015, pp. 275–278.

[55] B. Gray, J. S. Kenney, and R. Melville, "Behavioral modeling and simulation of a parametric power amplifier," in *IEEE MTT-S Int. Microw. Symp. Dig.*, Jun. 2009, pp. 1373–1376.

[56] B. Gray, B. Melville, and J. S. Kenney, "Analytical modeling of microwave parametric upconverters," *IEEE Trans. Microw. Theory Techn.*, vol. 58, no. 8, pp. 2118–2124, Aug. 2010.

[57] M. Masood, B. Gray, R. Melville, M. Omer, J. H. Chen, and J. S. Kenney, "Modeling and linearization of a parametric power upconverting amplifier," in *Proc. Eur. Microw. Conf. (EuMC)*, Sep. 2010, pp. 1026–1029.

[58] M. Pontón, A. Suárez, B. R. Gray, F. Ramírez, J. S. Kenney, and B. Melville, "In-depth stability analysis of degenerate parametric amplifiers," in *IEEE MTT-S Int. Microw. Symp. Dig.*, Jun. 2012, pp. 1–3.

[59] B. Gray, M. Pontón, A. Suárez, and J. S. Kenney, "Analytical modeling of transducer gain and gain compression in degenerate parametric amplifiers," in *Proc. IEEE Radio Wireless Symp. (RWS)*, Jan. 2012, pp. 351–354.

[60] A. Collado, A. Georgiadis, and A. Suarez, "Optimized design of retrodirective arrays based on self-oscillating mixers using harmonic-balance and conversion-matrix techniques," in *IEEE MTT-S Int. Microw. Symp. Dig.*, Jun. 2006, pp. 1125–1128.

[61] S. A. Maas, "Two-tone intermodulation in diode mixers," *IEEE Trans. Microw. Theory Techn.*, vol. MTT-35, no. 3, pp. 307–314, Mar. 1987.

[62] R. G. Meyer and M. L. Stephens, "Distortion in variable-capacitance diodes," *IEEE J. Solid-State Circuits*, vol. SSC-10, no. 1, pp. 47–54, Feb. 1975.

[63] S. I. Ghobrial, "Intermodulation distortion and gain compression in varactor frequency converters (Short Papers)," *IEEE Trans. Microw. Theory Techn.*, vol. MTT-23, no. 2, pp. 255–257, Feb. 1975.

[64] J. G. Gardiner and S. I. Ghobrial, "Distortion performance of the abrupt-junction current-pumped varactor frequency converter," *IEEE Trans. Microw. Theory Techn.*, vol. MTT-19, no. 9, pp. 741–749, Sep. 1971.

[65] J. G. Gardiner and S. I. Ghobrial, "Correction to 'distortion performance of the abrupt-junction current-pumped varactor frequency converter' (letters)," *IEEE Trans. Microw. Theory Techn.*, vol. MTT-20, no. 4, pp. 293–294, Apr. 1972.

[66] E. Markard, P. Levine, and B. Bossard, "Intermodulation distortion improvement in parametric upconverter," *Proc. IEEE*, vol. 55, no. 11, pp. 2060–2061, Nov. 1967.

[67] S. M. Perlow and B. S. Perlman, "A large signal analysis leading to intermodulation distortion prediction in abrupt junction varactor upconverters," *IEEE Trans. Microw. Theory Techn.*, vol. MTT-13, no. 6, pp. 820–827, Nov. 1965.

[68] D. R. Chambers and D. K. Adams, "A technique for the rapid calculation of distortion effects in varactor parametric amplifiers," in *Proc. G-MTT Int. Microw. Symp.*, May 1968, pp. 173–178.

[69] P. Penfield and R. Rafuse, *Varactor Applications*. Cambridge, MA, USA: MIT Press, 1962.

[70] W. F. Egan, *Practial RF System Design*. New York, NY, USA: Wiley, 2000.

[71] H. Khatri, P. S. Gudem, and L. E. Larson, "Distortion in current commutating passive CMOS downconversion mixers," *IEEE Trans. Microw. Theory Techn.*, vol. 57, no. 11, pp. 2671–2681, Nov. 2009.

[72] V. Asgari and L. Belostotski, "Wideband 28-nm CMOS variable-gain amplifier," *IEEE Trans. Circuits Syst. I, Reg. Papers*, vol. 67, no. 1, pp. 37–47, Jan. 2020.

[73] H. Zhang and E. Sanchez-Sinencio, "Linearization techniques for CMOS low noise amplifiers: A tutorial," *IEEE Trans. Circuits Syst. I, Reg. Papers*, vol. 58, no. 1, pp. 22–36, Jan. 2011.

[74] H. G. Han, D. H. Jung, and T. W. Kim, "A 2.88 mw+9.06 dbm IIP3 common-gate LNA with dual cross-coupled capacitive feedback," *IEEE Trans. Microw. Theory Tech.*, vol. 63, no. 3, pp. 1019–1025, Mar. 2015.

[75] S. Kabir, S. Magierowski, G. G. Messier, and Z. Zhao, "A direct 100 GHz parametric CMOS tripler," *IEEE Microw. Wireless Compon. Lett.*, vol. 23, no. 10, pp. 557–559, Oct. 2013.

[76] S. A. Maas, *Nonlinear Microwave Circuits*. New York, NY, USA: Artech House, 1996.

[77] Z. Zhao, S. Magierowski, and L. Belostotski, "Parametric CMOS upconverters and downconverters," *Int. J. Circuit Theory Appl.*, vol. 42, no. 12, pp. 1209–1227, Dec. 2014, doi: 10.1002/cta.1913.

[78] J.-F. B. S. Magierowski, T. Zourntos, and Z. Zhao, "Compact parametric downconversion using MOS varactors," in *IEEE MTT-S Int. Microw. Symp. Dig.*, Jun. 2009, pp. 1377–1380.

[79] H. E. Rowe, "Some general properties of nonlinear elements. II. Small signal theory," *Proc. IRE*, vol. 46, no. 5, pp. 850–860, May 1958.

[80] S. Magierowski, H. Chan, and T. Zourntos, "Subharmonically pumped RF CMOS paramps," *IEEE Trans. Electron Devices*, vol. 55, no. 2, pp. 601–608, Feb. 2008.

[81] Z. Zhao, S. Magierowski, and L. Belostotski, "Gain-configurable lower sideband parametric downconverter," in *Proc. 12th Eur. Microw. Integr. Circuits Conf. (EuMIC)*, Oct. 2017, pp. 113–116.

[82] Z. Zhao, J.-F. Bousquet, and S. Magierowski, "Coherent parametric RF downconversion in CMOS," in *Proc. IEEE Radio Freq. Integr. Circuits Symp. (RFIC)*, May 2010, pp. 377–380.

[83] *Guide to Harmonic Balance Simulation in ADS*, Adv. Design Syst. 2011.01 ed., Agilent Technol., Santa Clara, CA, USA, Feb. 2011.

[84] *Port Tutorial Series: Coplanar Waveguide (CPW)*, HFSS v8 ed., ANSOFT, Pittsburgh, PA, USA, 2002.

[85] *CMRF8SF Design Manual*, IBM, Endicott, NY, USA, 2007.

[86] D. M. Pozar, *Microwave Engineering*, 2nd ed. Hoboken, NJ, USA: Wiley, 1998.
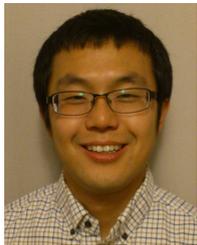
ZHIXING ZHAO received the M.Sc. degree in electrical engineering from the University of Calgary, Calgary, AB, USA, in 2011, where he is currently pursuing the Ph.D. degree. He had an Internship with IBM/GlobalFoundries, USA, from 2015 to 2016. He was involved in device characterizations and high-frequency tester designs. His research interests include CMOS high-frequency parametric circuitry design, such as parametric amplifier, mixer, and frequency multiplier.

SEBASTIAN MAGIEROWSKI (Member, IEEE) received the Ph.D. degree in electrical engineering from the University of Toronto, in 2004. From 2004 to 2012, he was a Faculty Member with the Department of Electrical and Computer Engineering, University of Calgary. His industrial experiences, such as Nortel Networks, PMC-Sierra, and Protolinx Corp. He also worked on CMOS device modeling, high-speed mixed-signal IC design, and data networks. In 2012, he joined the Department of Electrical Engineering and Computer Science, Lassonde School of Engineering, York University, Toronto, ON, Canada, where he is currently an Associate Professor. His research interests include analog/digital CMOS circuit design, communication systems, biomedical instrumentation, and signal processing for biomolecular sensing and analysis.

LEONID BELOSTOTSKI (Senior Member, IEEE) received the B.Sc. and M.Sc. degrees in electrical engineering from the University of Alberta, Edmonton, AB, Canada, in 1997 and 2000, respectively, and the Ph.D. degree from the University of Calgary, Calgary, AB, Canada, in 2007. He was a RF Engineer with Murandi Communications Ltd., Calgary, from 2001 to 2004. He is currently a Professor with the University of Calgary and the Canada Research Chair in high-sensitivity radiometers and receivers. His current research interests include RF and mixed-signal ICs, high-sensitivity receiver systems, antenna arrays, and terahertz systems. He was a recipient of the Outstanding Student Designer Award from Analog Devices Inc., in 2007, and the IEEE Microwave Theory and Techniques-11 Contest on Creativity and Originality in Microwave Measurements, in 2008. He serves as the IEEE Southern Alberta Solid-State, Circuits and Circuits and Systems Chapter's Chair. He served as an Associate Editor for the IEEE TRANSACTIONS ON INSTRUMENTATION AND MEASUREMENT. He serves as an Incoming Editor-in-Chief for *IEEE Solid-State Circuits Magazine*.

• • •